Eur. Phys. J. A (2020) 56:291
https://doi.org/10.1140/epja/s10050-020-00297-4

THE EUROPEAN PHYSICAL JOURNAL A

Regular Article - Experimental Physics

Lifetimes of core-excited states in semi-magic ^{95}Rh

A. Ertoprak[1,2,a], C. Qi[1], B. Cederwall[1], M. Doncel[1,3], U. Jakobsson[1,4], B. M. Nyakó[5], G. Jaworski[6,7], P. Davies[8], G. de France[9], I. Kuti[5], D. R. Napoli[6], R. Wadsworth[8], S. S. Ghugre[10], R. Raut[10], B. Akkus[2], H. Al Azri[8], A. Algora[5,11], G. de Angelis[6], A. Atac[1], T. Bäck[1], A. Boso[12], E. Clément[9], D. M. Debenham[8], Zs. Dombrádi[5], S. Ertürk[13], A. Gadea[11], F. Ghazi Moradi[1], A. Gottardo[14], T. Hüyük[11], E. Ideguchi[15], H. Li[1], C. Michelagnoli[9], V. Modamio[6], J. Nyberg[16], M. Palacz[7], C. M. Petrache[14], F. Recchia[12], M. Sandzelius[17], M. Siciliano[6], D. Sohler[5], J. Timár[5], J. J. Valiente-Dobón[6], Z. G. Xiao[18]

[1] Department of Physics, Royal Institute of Technology (KTH), 10691 Stockholm, Sweden
[2] Department of Physics, Faculty of Science, Istanbul University, Vezneciler/Fatih, 34134 Istanbul, Turkey
[3] Oliver Lodge Laboratory, Department of Physics, University of Liverpool, Liverpool L69 7ZE, UK
[4] Department of Chemistry, University of Helsinki, P.O. Box 3, 00014 Helsinki, Finland
[5] Institute for Nuclear Research (Atomki), P.O. Box 51, Debrecen 4001, Hungary
[6] Istituto Nazionale di Fisica Nucleare, Laboratori Nazionali di Legnaro, 35020 Legnaro, Italy
[7] Heavy Ion Laboratory, University of Warsaw, Pasteura 5A, 02-093 Warsaw, Poland
[8] Department of Physics, University of York, Heslington, York YO10 5DD, UK
[9] Grand Accélérateur National d'Ions Lourds (GANIL) CEA/DSM - CNRS/IN2P3, Bd Henri Becquerel BP 55027, 14076 Caen Cedex 5, France
[10] UGC-DAE Consortium for Scientific Research, Kolkata Centre, Kolkata 700098, India
[11] Instituto de Física Corpuscular, CSIC-Universidad de Valencia, 46980 Valencia, Spain
[12] Dipartimento di Fisica e Astronomia, Università di Padova, Padova, Italy
[13] Science and Art Faculty, Department of Physics, Nigde Omer Halisdemir University, 51200 Nigde, Turkey
[14] Université Paris-Saclay, CNRS/IN2P3, IJCLab, 91405 Orsay, France
[15] Research Center for Nuclear Physics, Osaka University, Osaka, Japan
[16] Department of Physics and Astronomy, Uppsala University, 75120 Uppsala, Sweden
[17] Department of Physics, University of Jyväskylä, 40014 Jyväskylä, Finland
[18] Department of Physics, Tsinghua University, Beijing 100084, China

Received: 15 June 2020 / Accepted: 2 November 2020 / Published online: 17 November 2020

Communicated by Wolfram Korten

Abstract Lifetimes of negative-parity states have been determined in the neutron deficient semi-magic (N = 50) nucleus ^{95}Rh. The fusion-evaporation reaction $^{58}Ni(^{40}Ca, 3p)$ was used to populate high-spin states in ^{95}Rh at the Grand Accélérateur National d'Ions Lourds (GANIL) accelerator facility. The results were obtained using the Doppler Shift Attenuation Method (DSAM) based on the Doppler broadened line shapes produced during the slowing down process of the residual nuclei in a thick 6 mg/cm^2 metallic target. B(M1) and B(E2) reduced transition strengths are compared with predictions from large-scale shell-model calculations.

1 Introduction

The structure of atomic nuclei near the $N = Z = 50$ shell closures has received special attention in current nuclear structure research, providing unique opportunities to test state-of-the-art theory. Remarkably, the structural features up to moderate angular momentum of nuclei immediately below the $N = Z = 50$ shell closures can be described with high accuracy in a very simple way by shell-model calculations including only the $g_{9/2}$ and $p_{1/2}$ subshells. Of special interest is the neutron-proton pair coupling scheme which is expected to appear in the heaviest N=Z nuclei [1,2] and the seniority structure of the $N = 50$ isotones [3–7]. However, multiple core-excited states have been observed in the semi-magic nuclei of the ^{100}Sn region [8–10]. The theoretical study of those states is a challenging task, which requires a significantly larger model space for their interpretation. Transition probabilities between nuclear states provide important constraints for theoretical modelling of the structure of the nuclei of interest. Our previous lifetime study of the semi-magic ($N = 50$) nucleus ^{94}Ru [11,12] provided information on the electromagnetic decay properties of neutron-core excited states. We now address lifetime measurements in its closest, more neutron deficient, isotone ^{95}Rh using the

[a] e-mail: ertoprak@kth.se (corresponding author)

same DSAM technique. The experimental results have been interpreted within the framework of large-scale shell-model (LSSM) calculations.

2 Experimental set-up

The experiment was performed at the Grand Accélérateur National d'Ions Lourds (GANIL), Caen, France. High-spin states in ^{95}Rh were populated using the ^{58}Ni(^{40}Ca, $3p$)^{95}Rh heavy-ion fusion-evaporation reaction. The beam of ^{40}Ca ions was accelerated by the CSS1 cyclotron of GANIL to a kinetic energy of 150 MeV and subsequently degraded to 128 MeV in a thin Ta foil in front of the production target. The energy degraded beam was used to bombard target foils consisting of 99.9% isotopically enriched ^{58}Ni targets of thickness $\sim$ 6 mg/cm^2, thick enough to stop the fusion residues. The total irradiation time was 14 days with an average beam intensity of 7 particle nanoamperes (pnA). The experimental set-up consisted of the EXOGAM germanium detector array [13], the DIAMANT charged particle detector system [14,15] and the Neutron Wall liquid scintillator array [16]. Prompt γ rays from the reaction products were detected by EXOGAM in its compact configuration consisting of 11 Compton-suppressed clover HPGe detectors. Seven detectors were positioned at an angle of 90° and four detectors at an angle of 135° relative to the beam axis. The total photopeak efficiency was 11% at 1.3 MeV. Light charged-particle emission following the formation of the compound nucleus ^{98}Cd was detected by the 4π DIAMANT detector system which consisted of 80 CsI(Tl) scintillators. Evaporated neutrons were detected by the Neutron Wall array of 50 BC501 A [17,18] liquid-scintillator detectors covering a 1π solid angle in the forward direction. The detection efficiency of the Neutron Wall for the evaporated neutrons was around 25% while the proton and α particle efficiencies of DIAMANT were around 55% and 48%, respectively.

The radio frequency signal from the cyclotron accelerator was utilised as a time reference for the time-of-flight signal. The hardware trigger condition for recording events for subsequent offline analysis was fulfilled in the case of one detected γ-ray in any of the Ge detectors together with one neutron-like event registered in the Neutron Wall. The condition for the neutron-like events was determined by the pulse shape of the organic liquid scintillator detector signals. This hardware threshold was sufficiently relaxed to allow also a substantial fraction of neutron-less events, in particular corresponding to the ^{95}Rh, to be collected. The energy and efficiency calibrations were carried out with standard radioactive sources (^{60}Co and ^{152}Eu).

3 Data analysis and results

In the offline analysis, relative γ-ray intensities and branching ratios for electromagnetic transitions belonging to ^{95}Rh were analysed using the RADWARE software package [19]. The up to date published information on the known excited states in ^{95}Rh can be found in Ref. [20]. The γ-rays were emitted from the recoiling ^{95}Rh nuclei while they were slowing down or stopped inside the target which was sufficiently thick to stop the recoils. Hence, Doppler broadened lineshapes were produced for γ rays de-exciting states with lifetimes of the order of the stopping time in the target material (around 1–2 ps) or shorter. The Doppler Shift Attenuation Method (DSAM) was used to deduce level lifetimes from the observed Doppler-broadened line shapes [21]. Standard DSAM measurements are conventionally performed with a thin target on a high-Z backing material. The thin target facilitates the analysis by allowing the assumption that the beam energy is approximately constant throughout the expanse of the target and, consequently, the cross-section for production of the residue of interest is constant therein. In the case of a thick homogeneous target, there is a significant change (decrease) in the energy of the beam particles while they are traversing the target, resulting in a variation in the production cross-section as a function of the depth of the target. As the energy (128 MeV) of the ^{40}Ca beam incident on the ^{58}Ni target, is just below the effective Coulomb barrier, a significant fraction of the fusion products are essentially produced in the first thin layer ($\sim$ 1 mg/cm^2) of the target. The cross-section for the ^{95}Rh residues drops rapidly within this layer while the remaining thickness of the target effectively acted only as a stopping medium, i.e. as the "backing" in conventional DSAM measurements. The fusion cross-section as a function of beam energy can be obtained from experimental data and/or calculated using statistical model calculations, using available statistical model codes, such as the PACE4 [22]. Since the fusion cross-section changes drastically with beam energy around the Coulomb barrier a DSAM measurement at these energies requires incorporation of these effects, contrary to the conventional practice of assuming a uniform cross-section throughout the target. Here, the residue production cross-section as a function of the beam energy was taken from the detailed measurements by Bourgin et al. [23].

The lifetime analysis was carried out using a modified version of the LINESHAPE [24] computer program, see Ref. [25]. This incorporates the aforementioned variation in the residue cross-section within the target as well as updated stopping powers computed by the SRIM code [26,27] for the calculation of the velocity profiles of fusion residues in the target medium. The code was used to calculate the Doppler broadened line shapes of the transition peaks of interest and to perform least-square fits to the experimental spectra in order to obtain the corresponding level lifetimes (τ). The

analysis has been detailed in our previous papers on the lifetime investigations in ^{94}Ru [11,12]. In the germanium energy spectra, there are intrinsic peak shape asymmetries as a result of charge trapping which was taken into account in the fitting function during the lifetime analysis. The Narrow Gate on Transition Below (NGTB) procedure [21] was also used to eliminate the effects of detector-related line shape asymmetries on the deduced lifetime values. The NGTB method has to be used with extra care at 90° spectra since the tail can move in towards the centre of the peak, but the gate can avoid the tail. This has been taken into account carefully in the lifetime analysis.

Side feeding and feeding from higher-lying excited states have to be carefully taken into account in the analysis. For this reason, branching ratios for the γ-decays into and out of the states of interest were studied in detail (Table 1). Figure 1 shows the relevant part of the level scheme of ^{95}Rh deduced

Table 1 Relative γ-ray intensities for ^{95}Rh measured in the present work

Negative parity		
$I_i^\pi \rightarrow I_f^\pi$	E_γ (keV)	I_γ
$37/2_1^- \rightarrow 35/2_1^-$	261.3 (2)	167 (3)
$29/2_2^- \rightarrow 29/2_1^-$	293.8 (3)	32 (2)
$(31/2_1^-) \rightarrow (29/2_3^-)$	331.8 (3)	13 (1)
$33/2_1^- \rightarrow 31/2_3^-$	333.9 (2)	78 (2)
$29/2_4^- \rightarrow 27/2_2^-$	448.2 (2)	44 (5)
$31/2_3^- \rightarrow 29/2_4^-$	479.9 (2)	54 (3)
$35/2_1^- \rightarrow 33/2_1^-$	549.3 (2)	251 (3)
$27/2_2^- \rightarrow (25/2_2^-)$	611.3 (3)	39 (3)
$25/2_1^- \rightarrow 21/2_1^-$	667.9 (1)	515 (6)
$39/2_1^- \rightarrow 37/2_1^-$	691.0 (1)	194 (3)
$29/2_4^- \rightarrow (25/2_4^-)$	721.6 (2)	10 (3)
$37/2_1^- \rightarrow 33/2_1^-$	810.1 (2)	58 (2)
$31/2_3^- \rightarrow 29/2_2^-$	813.4 (2)	91 (3)
$(29/2_3^-) \rightarrow 27/2_1^-$	876.5 (3)	26 (2)
$39/2_1^- \rightarrow 35/2_1^-$	953.0 (4)	19 (4)
$(39/2_2^-) \rightarrow 37/2_1^-$	1015.9 (3)	23 (3)
$33/2_1^- \rightarrow 29/2_2^-$	1147.4 (1)	200 (7)
$41/2_1^- \rightarrow 39/2_1^-$	1307.1 (5)	12 (4)
$41/2_1^- \rightarrow 37/2_1^-$	1998.1 (4)	13 (2)
$(41/2_2^-) \rightarrow 39/2_1^-$	2021.9 (3)	6 (1)
$27/2_1^- \rightarrow 25/2_1^-$	2038.1 (2)	13 (1)
$(25/2_2^-) \rightarrow 25/2_1^-$	2066.4 (2)	10 (2)
$(25/2_3^-) \rightarrow 25/2_1^-$	2279.9 (3)	9 (2)
$(25/2_4^-) \rightarrow 25/2_1^-$	2403.3 (2)	12 (2)
$29/2_1^- \rightarrow 25/2_1^-$	2496.0 (2)	41 (2)
$27/2_2^- \rightarrow 25/2_1^-$	2677.0 (3)	34 (3)
$29/2_2^- \rightarrow 25/2_1^-$	2790.0 (1)	130 (4)

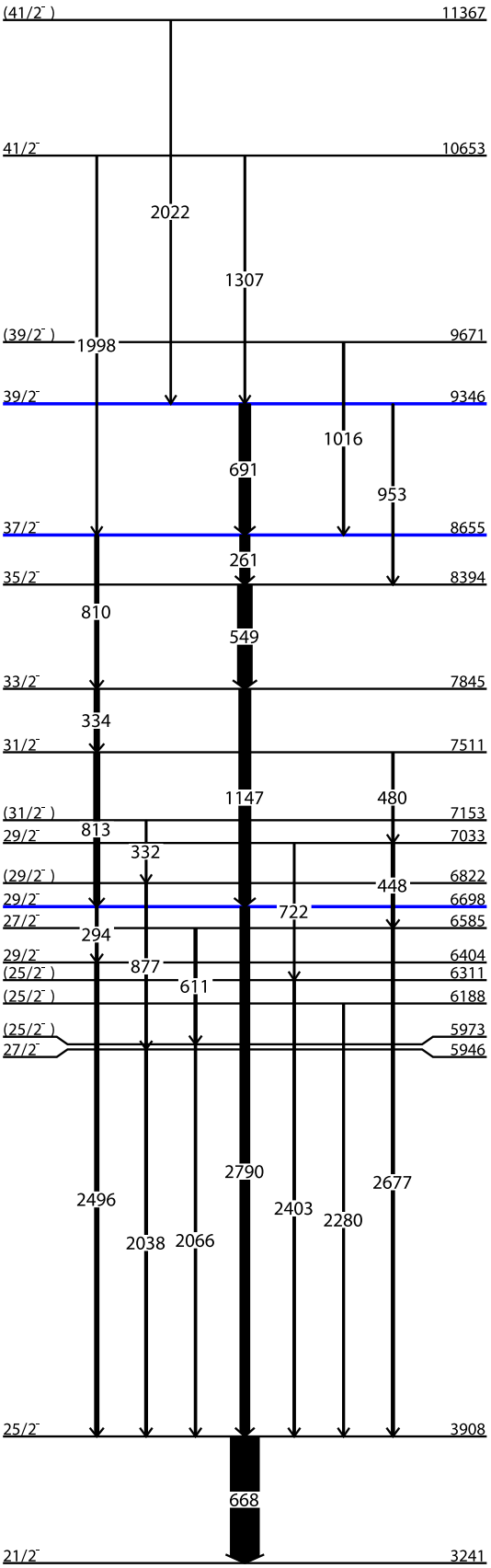

Fig. 1 Partial level scheme of ^{95}Rh highlighting the levels for which lifetime values were obtained in the present work in blue. Spin-parity assignments are taken from Ref. [20]

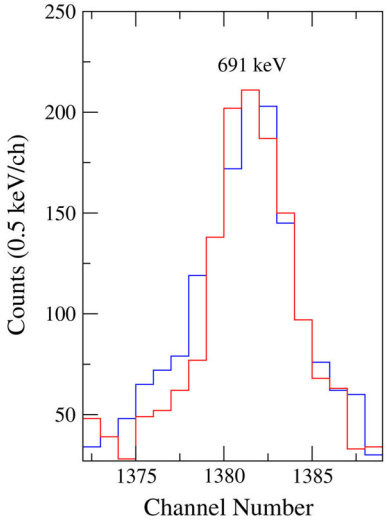

Fig. 2 Comparison between the experimental γ-ray energy spectra for the 691 keV transition ($39/2_1^- \rightarrow 37/2_1^-$) for gates set on the 2022 keV direct feeding transition of the in-flight (blue) and stopped (red) components of the Doppler broadened lineshapes

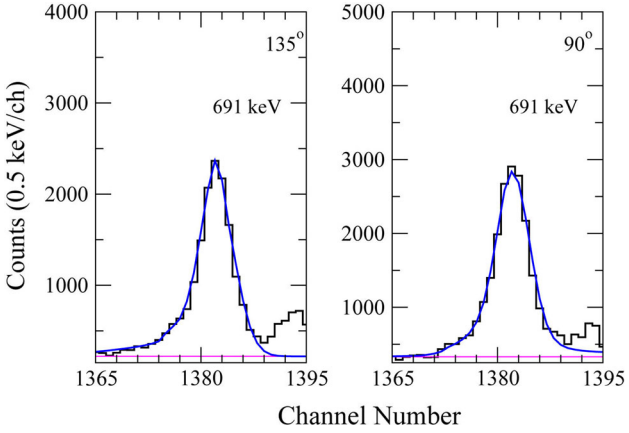

Fig. 3 Experimental γ-ray energy spectra and corresponding lineshape fits for the 691.0 keV ($39/2_1^- \rightarrow 37/2_1^-$) transition. The spectra demonstrate the Doppler broadened line shapes at 135° and 90° relative to the beam axis (left and right panel, respectively) obtained by a narrow gate on the stopped component of the 549 keV ($35/2_1^- \rightarrow 33/2_1^-$) transition. The lifetime value of the $39/2_1^-$ state deduced from the present work, 0.94(9) ps, is within the upper limit (< 1.4 ps) reported by Jungclaus et al. [28]

from the present work. In the present work, lifetime analyses for the $29/2_2^-$, $37/2_1^-$ and $39/2_1^-$ states in ^{95}Rh have been performed and compared with previously reported values and limits obtained using the recoil distance Doppler shift (RDDS) technique [28].

The lifetime result that we reported for the 18^+ state in the ^{94}Ru nucleus [11] is in agreement with the previous measurement [29] using a different (RDDS) technique providing confidence in the validity of the special use of the DSAM technique in this work. Figure 2 shows the Doppler broadened lineshapes of the 691 keV ($39/2_1^- \rightarrow 37/2_1^-$) transition obtained by gating on the in-flight and the stopped components of the 2022 keV ($(41/2_2^-) \rightarrow 39/2_1^-$) transition, directly feeding the $39/2_1^-$ state, respectively. An enhancement of the Doppler broadening can be seen on the low-energy side of the peak obtained by gating on the flight component of the feeding transition.

Due to the low beam energy, many of the medium and high-spin states of interest receive significant amounts of direct feeding. For example, the $39/2_1^-$ excited state at 9346 keV has previously been observed to have discrete feeding transitions from states that are situated at around 2.1–3.6 MeV higher in excitation energy [8]. None of these feeding transitions were observed in the present experiment, presumably due to the significantly lower excitation energy attainable in the present reaction. It is also noteworthy that the 2022 keV $(41/2_2^-) \rightarrow 39/2_1^-$ transition is here observed at a relative intensity of around 3% compared with the intensity of the transitions depopulating the $39/2_1^-$ state. The corresponding value found in Ref. [8] was 21%. It is therefore reasonable to assume that the $39/2_1^-$ excited state predominantly receives direct, very fast feeding and that unobserved feeding from discrete states can be safely neglected in the analysis. Previously measured lifetimes of excited states situated below the $39/2_1^-$ state, are also well reproduced in the present work assuming direct, fast feeding of the $39/2_1^-$ state. An iterative process was adopted in such a way that once the lifetime of a certain state had been determined it was used as an input value for the next lower level in the γ-ray cascade, and so on. Intermediate verification could be obtained from known lifetime values, for example of the $37/2_1^-$ excited state, reported by Jungclaus et al. [28]. As can be seen in Table 2, the limit established for the $39/2^-$ excited state in Ref. [8] is in agreement with the lifetime value obtained from the present measurement.

In the lifetime analysis, the γ-ray energy spectra detected at 90° and 135° relative to the beam axis were fitted simultaneously using a common χ^2 minimisation procedure. Fig. 3 shows the relevant part of the spectra observed in the detectors positioned at 135° and 90°, respectively. For the determination of the lifetime of the $39/2_1^-$ excited state, the lifetime value determined for the $41/2^-$ excited state as well as the lifetime value of the previously tentatively assigned $(41/2^-)$ excited state have been taken into account, giving a value of 0.94(9) ps in agreement with the limit < 1.4 ps given in Ref. [28]. The statistical uncertainties are around 10%. Additionally, systematic uncertainties in the present measurements are considered to be dominated by the employed stopping powers. Lifetime values deduced using different stopping power tables (Ziegler at al. [26,27] and Northcliffe and Schilling [30], respectively) were therefore compared, keeping the other fitting conditions the same. It was found

Table 2 Lifetime values of excited states in ^{95}Rh obtained from the present work and in comparison with previously measured values and limits. The initial level excitation energy (E_x), spin-parity assignments and γ-ray transition energy (E_γ) are given in the first, second, and third column, respectively. Lifetime values, τ, investigated through DSAM in the present work are given in column 4 while the lifetime results from Ref. [28] is shown in column 5. Uncertainties (statistical) are given within parentheses. Relative systematic uncertainties due to the modelling of stopping powers are estimated to be approximately 10% or less

E_x (keV)	$I_i^\pi \rightarrow I_f^\pi$	E_γ (keV)	τ(ps)	τ_{lit}(ps)
9346	$39/2_1^- \rightarrow 37/2_1^-$	691.0 (1)	0.94 (9)	< 1.4
8655	$37/2_1^- \rightarrow 35/2_1^-$	261.3 (2)	1.64(21)	1.67(32)
6698	$29/2_2^- \rightarrow 25/2_1^-$	2790.0 (1)	1.28 (13)	1.23 (7)

that the resulting excited-state lifetimes varied within 10% and the associated mean variation is substantially less. Consequently, we assume that 10% is a conservative estimate of the relative systematic uncertainties due to stopping powers.

We have also measured the lifetime values of the $37/2_1^-$ excited state at 8655 keV and the $29/2_2^-$ excited state at 6698 keV, being consistent with the RDDS results obtained by Junglaus et al. [28]. The results of the lifetime analysis are shown in Table 2.

4 Discussion

The structure of the low-lying states in ^{95}Rh is expected to be similar to that of ^{94}Ru and is built primarily on proton single-particle structures from the $g_{9/2}$ and $p_{1/2}$ subshells. Earlier shell model calculations (see, for example, Ref. [28]) suggest that the yrast and near-yrast positive-parity and negative-parity structures are dominated by the $\pi(g_{9/2}^{-5})$ and $\pi(p_{1/2}^{-1}g_{9/2}^{-4})$ configurations, respectively. This conclusion is also supported by our previous LSSM calculation [20] in the extended space including proton and neutron orbitals $p_{3/2,1/2}$, $f_{5/2}$, $g_{9/2,7/2}$ and $d_{5/2}$. In that paper, we introduced a new realistic effective Hamiltonian constructed in particular for the large model space. For the agreement between calculated and experimental level energies was seen to be quite good for yrast states up to relatively high angular momentum $I \sim 20\hbar$. Details can be found in Ref. [20] and the present manuscript will focus only on the reduced transition probabilities. As for the negative-parity group, the maximal spin one can build in the $p_{1/2}g_{9/2}$ space is $25/2$. Most of the states above $25/2_1^-$ show significant contribution from neutron $\nu(d_{5/2}g_{9/2}^{-1})$ core excitations. In the nucleus ^{94}Ru, the yrast 20^- state has been shown to be dominated by the maximally spin-aligned state of the $\pi(p_{1/2}^{-1}g_{9/2}^{-5}) \otimes \nu(d_{5/2}g_{9/2}^{-1})$ configuration [12]. This state lies more than 1 MeV lower in energy than the next $I = 20\hbar$ state and receives most of the intensity flowing from the higher-lying states via multiple transitions. One can expect that the $39/2_1^-$ state in ^{95}Rh is analogous to that state and is dominated by the maximally aligned configuration $\pi(p_{1/2}^{-1}g_{9/2}^{-4}) \otimes \nu(d_{5/2}g_{9/2}^{-1})$. The states lying just below $39/2_1^-$ are calculated to have similar structure. The B(M1) value for the $33/2_1^- \rightarrow 31/2_1^-$ transition is significantly underestimated by all shell model calculations presented in the table. We suspect that the observed $31/2_1^-$ state may actually be a mixture of the calculated lowest two states. Those two states have different structure which can be seen from the fact that the M1 decay to the second state is vanishing.

We have recalculated the wave functions for negative-parity states with spin values between $21/2$ and $39/2$ in the extended model space with the same Hamiltonian as introduced in Ref. [20] in which only the predicted excited-state energies were reported. In the present work, we are interested in testing the accuracy of the LSSM wave function and the prediction power of the model in electromagnetic transition probabilities. Therefore, we calculated the lowest three states for each spin and then all possible electromagnetic transitions among them. As shown in [20], the LSSM calculation predicts very well the energies of most states in ^{95}Rh including the non-yrast states. The experimental state with 9671 keV energy is tentatively assigned as $39/2_2^-$ in Ref. [20]. This state is not reproduced in the LSSM calculation where the second $39/2^-$ state is calculated to be as much as 1.4 MeV higher than the yrast state.

As discussed in Ref. [12], M1 transitions offer special opportunities to test the many-body wave function. In particular for cross orbital excitations, the magnetic dipole operator only links single-particle orbitals with the same principal quantum number and orbital angular momentum (spin-orbit partners with the same l) [28]. As a result, similarly to the case of ^{94}Ru, the M1 transition properties can be expected to be dominated by coupling within the $g_{9/2}$ subshell and the possible excitation of nucleons from $g_{9/2}$ to its $g_{7/2}$ spin-orbit partner across the $N = 50$ shell gap. The g-factor for states involving these orbitals is significantly larger compared with those of $p_{1/2}$ or $p_{3/2}$ within the $N = 28 - 50$ shell. The results of our measurements on the M1 transition strengths are given in Table 3 assuming negligible E2 admixtures. The estimated admixture from E2 is on the order of 10^{-6} to 10^{-7}. For the calculations of B(M1) reduced transition strengths we used both the bare and the effective spin gyromagnetic factors

Table 3 Experimental $[B(M1)_{exp}$ and $B(E2)_{exp}]$ reduced transition probabilities in ^{95}Rh obtained from present measurement. $B(M1)_{exp2}$ and $B(E2)_{exp2}$ values are from the lifetime measurement of Ref. [28] and given in column 7. The subscripts "th1" and "th2" correspond to predictions from large-scale shell-model calculations carried out in this work using effective and bare g factors and are given in columns 8 and 9, respectively. Results of shell model calculations from Ref. [28] are denoted as "th3" and given in column 10. Statistical uncertainties on the experimental values are given within parentheses. *The measurement is not sensitive to any E2 admixture. Therefore, the transitions are classified as M1

E_x [keV]	I_i^π	E_γ [keV]	I_f^π	σL	$B(M1\downarrow)_{exp^*}$ $[10^{-3}\mu_N{}^2]$	$B(M1\downarrow)_{exp2}$ $[10^{-3}\mu_N{}^2]$	$B(M1\downarrow)_{th1}$ $[10^{-3}\mu_N{}^2]$	$B(M1\downarrow)_{th2}$ $[10^{-3}\mu_N{}^2]$	$B(M1\downarrow)_{th3}$ $[10^{-3}\mu_N{}^2]$
9346	$39/2_1^-$	691.0	$37/2_1^-$	M1	167(16)	> 107	225	402	427
	$39/2_1^-$		$37/2_2^-$	M1			2092	2919	
	$39/2_1^-$		$37/2_3^-$	M1			833	1395	
8655	$37/2_1^-$	261.3	$35/2_1^-$	M1	1678(215)	1664(338)	1308	2000	1100
	$37/2_1^-$		$35/2_2^-$	M1			222	381	
	$37/2_1^-$		$35/2_3^-$	M1			99	79	
8394	$35/2_1^-$	549.3	$33/2_1^-$	M1		116(13)	276	485	440
	$35/2_1^-$		$33/2_2^-$	M1			1202	1808	
	$35/2_1^-$		$33/2_3^-$	M1			571	672	
7845	$33/2_1^-$		$31/2_1^-$	M1			7	22	
	$33/2_1^-$	333.9	$31/2_2^-$	M1		172(28)	929	1388	839
	$33/2_1^-$		$31/2_3^-$	M1			1	2	

E_x [keV]	I_i^π	E_γ [keV]	I_f^π	σL	$B(E2\downarrow)_{exp}$ $[e^2fm^4]$	$B(E2\downarrow)_{exp2}$ $[e^2fm^4]$	$B(E2\downarrow)_{th1}$ $[e^2fm^4]$	$B(E2\downarrow)_{th3}$ $[e^2fm^4]$
9346	$39/2_1^-$	953.0	$35/2_1^-$	E2	98(10)	> 124	71	284
	$39/2_1^-$		$37/2_1^-$	E2			37	
8655	$37/2_1^-$	810.1	$33/2_1^-$	E2	171(22)	154(63)	112	277
	$37/2_1^-$		$35/2_1^-$	E2			10	
	$35/2_1^-$		$31/2_1^-$	E2			129	
	$35/2_1^-$		$33/2_1^-$	E2			46	
	$33/2_1^-$		$31/2_1^-$	E2			2.3	
	$29/2_1^-$		$25/2_1^-$	E2			142	
6698	$29/2_2^-$	2790.0	$25/2_1^-$	E2	2.32(24)	3.1(3)	33.5	0.73
	$29/2_3^-$		$25/2_1^-$	E2			2.97	
	$27/2_1^-$		$25/2_1^-$	E2			28.8	
	$27/2_2^-$		$25/2_1^-$	E2			6.79	
	$27/2_3^-$		$25/2_1^-$	E2			0.602	
3908	$25/2_1^-$	667.9	$21/2_1^-$	E2		172 (12)	540	341

with $g_s = 0.7 \cdot g_s(\text{free})$. The calculation with the effective g factor reproduces the observed $B(M1)$ value excellently for the transition $39/2^- \rightarrow 37/2^-$, similarly to the observation for the analogous transitions in ^{94}Ru [12]. The good agreement between the experiment and calculation supports the assumption that those states should be dominated by the simple spin-aligned configurations mentioned above. In addition, strong M1 transitions between the $39/2_1^-$ and the second $37/2^-$ state and between the $37/2_1^-$ and $35/2_1^-$ states are predicted in the calculation. The latter result is in agreement with earlier measurement, as shown in Table 2. Our prediction should be compared with future measurements on the $39/2_1^- \rightarrow 37/2_2^-$ half life. We have also done calculations within the restricted $\pi(p_{1/2}^{-1}g_{9/2}^{-4}) \otimes \nu(d_{5/2}g_{9/2}^{-1})$ model space in order to understand the role of neutron excitations to $d_{5/2}$ and $g_{7/2}$. In those calculations, we applied the same effective interaction as in our LSSM calculation but restricted the particle excitations to be only within the four orbitals. The other orbitals, in particular $g_{7/2}$, are left frozen. The calculated results for $B(M1; 39/2_1^- \rightarrow 37/2_1^-)$ are nearly the same as those from the LSSM calculation. It should be mentioned that the maximal spin one can build from the $g_{9/2}^{-4}$ configuration is 12, which corresponds to a unique state with a pure seniority-four wave function [31]. The next largest

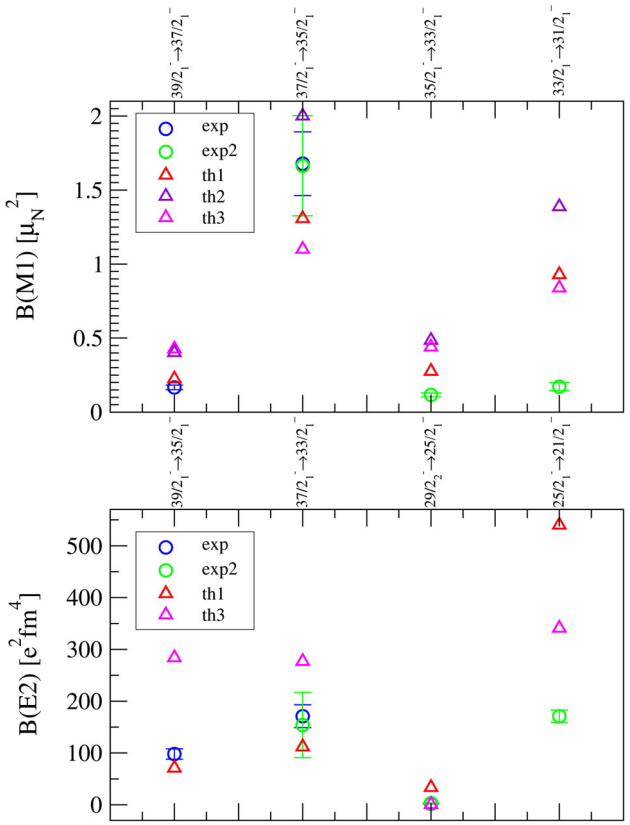

Fig. 4 Comparison between experimental B(M1) and B(E2) transition strengths and predictions by large-scale shell model calculations for ^{95}Rh

spin value is 10. It is not possible to form 11^+ solely from that $g_{9/2}^{-4}$ configuration. That indicates that the $37/2^-$ states shown in the table can only be built from the configurations based on $\pi(p_{1/2}^{-1}g_{9/2}^{-4;J=12})\otimes\nu(d_{5/2}g_{9/2}^{-1})$[6,7]. Our calculations show that the B(M1) value is indeed sensitive to the mixture of those configurations. A large $B(M1; 39/2_1^- \rightarrow 37/2_1^-)$ is expected if the aligned $\pi g_{9/2}$ component is enhanced in the $37/2_1^-$ state. The transitions between $37/2^-$ and the first two $35/2^-$ states show a similar sensitivity, even though in those cases the decay to the first $35/2^-$ state is favoured instead in the original calculation.

We have also calculated the B(E2) values for transitions involving those states. We took $e_p = 1.5e$ and $e_n = 0.8e$ for the effective charges which reproduce the E2 transition properties well for neighbouring nuclei just below or above the $N = Z = 50$ shell closure [32–34]. The results for transitions among yrast states are also shown in the table. $B(M1)$ and $B(E2)$ values extracted from the present lifetime analysis are compared with the large-scale shell model calculations in Fig. 4. Shell model calculations were also presented in Ref. [28] within the model space $\pi(p_{3/2,1/2}, f_{5/2}, g_{9/2})$ and $\nu g_{9/2}, d_{5/2}$. Those calculations also showed that the core-excited states are dominated by the neutron $\nu g_{9/2} \rightarrow d_{5/2}$ excitation. In the calculations of the EM transitions, they used the same effective g factor as in our case "th2" but adopted unusually large effective charges for protons and neutrons ($e_p = 1.72e$ and $e_n = 1.44e$). Part of their results are also shown in the table marked as "th3". The dominating components of the calculated wave functions were also given in Ref. [28] which agree with our results in general. A noticeable difference concerns the contribution from the $f_{5/2}$ orbital which is predicted to be significantly larger in Ref. [28] than in our calculations. In particular, the $29/2_1^-$ state was calculated to be dominated by $\pi(f_{5/2}^{-1}g_{9/2}^{-4})$ in Ref. [28] but by $\pi(p_{1/2}^{-1}g_{9/2}^{-4})$ in ours.

5 Summary

High-spin states of the ^{95}Rh semi-magic nucleus were populated via the fusion-evaporation reaction ^{58}Ni(^{40}Ca, $3p$). Lifetime values for the negative-parity states have been obtained from an analysis of the Doppler broadened line shapes using the DSAM technique. Large-scale shell-model calculations have been performed to interpret the electromagnetic decay properties of ^{95}Rh and to compare with earlier calculations employing more restricted model spaces. We found that many of the observed high-lying states are well described by a simple one-neutron cross-shell excitation.

Acknowledgements We thank the operators of the GANIL cyclotrons for providing the beam, their cooperation and technical support. We would also like to thank the EXOGAM, DIAMANT and Neutron Wall Collaborations. This work was supported by the Swedish Research Council under Grant Nos. 621-2014-5558, 621-2012-3805, and 621-2013-4323 and the Göran Gustafsson foundation, the Scientific Research Projects Coordination Unit of Istanbul University Project No. 47886 and 48101, the UK STFC under grants number ST/L005727/1 and ST/P003885/1, the Spanish Ministerio de Economía y Competitividad under grant FPA2014-52823-C2-1-P and the program Severo Ochoa (SEV-2014-0398), Ministerio de Ciencia e Innovación, and Generalitat Valenciana, Spain, under the Grants FPA2017-84756-C4, PROMETEO/2019/005 and by the EU FEDER funds, the Scientific and Technological Council of Turkey (Proj. no. 114F473), the National Science Centre, Poland (NCN), 2017/25/B/ST2/01569, 2016/22/M/ST2/00269, 2013/08/M/ST2/00257, COPIGAL and COPIN-IN2P3 projects. B.M.Ny., I.K., Zs.D. and J.T. acknowledge the support of the National Research, Development and Innovation Fund of Hungary, financed under the K18 funding scheme with project no. K128947, as well as by the European Regional Development Fund (Contract No. GINOP-2.3.3-15-2016-00034), while I.K. was also supported by the National Research, Development and Innovation Office NKFIH, contract number PD 124717. The computations were performed on resources provided by the Swedish National Infrastructure for Computing (SNIC) at PDC, KTH, Stockholm.

Funding Open access funding provided by Royal Institute of Technology.

Data Availability Statement This manuscript has no associated data or the data will not be deposited. [Authors' comment: All data generated during this study are contained in this published article.]

References

1. B. Cederwall et al., Nature **68**, 469 (2011)
2. C. Qi, J. Blomqvist, T. Bäck, B. Cederwall, A. Johnson, R.J. Liotta, R. Wyss, Phys. Rev. C **84**, 021301 (2011)
3. A. Escuderos, L. Zamick, Phys. Rev. C **73**, 044302 (2006)
4. P. Van Isacker, S. Heinze, Phys. Rev. Lett. **100**, 052501 (2008)
5. C. Qi et al., Phys. Rev. C **83**, 014307 (2011)
6. C. Qi et al., Nucl. Phys. A **21**, 884 (2012)
7. C. Qi et al., Phys. Lett. B **773**, 616 (2017)
8. H.A. Roth et al., Phys. Rev. C **50**, 1330 (1994)
9. M. Palacz et al., Phys. Rev. C **86**, 014318 (2012)
10. M. Lipoglavsek et al., Phys. Rev. Lett. **76**, 888 (1996)
11. A. Ertoprak, B. Cederwall, C. Qi et al., Acta Phys. Pol. **B48**, 325 (2017)
12. A. Ertoprak, B. Cederwall, C. Qi et al., Eur. Phys. J. **A54**, 145 (2018)
13. J. Simpson et al., Acta Phys. Hung. New Ser: Heavy Ion Phys. **11**, 59 (2000)
14. J.N. Scheurer et al., Nucl. Instr. Methods Phys. Res. Sect. A **385**, 501 (1997)
15. J. Gál et al., Nucl. Instr. Meth. A **516**, 502 (2004)
16. O. Skeppstedt et al., Nucl. Instr. Meth. A **421**, 531 (1999)
17. Saint Gobain Cristals, USA, BC501/BC501A/BC519, https://www.crystals.saint-gobain.com/products/bc-501a-bc-519. Accessed 12 Nov 2020
18. R.A. Cecil, B.D. Anderson, R. Madey, Nucl. Instrum. Methods Phys. Res. **161**, 439 (1979)
19. D. Radford, Nucl. Instr. Meth. A **361**, 297 (1995)
20. F.G. Moradi, C. Qi, B. Cederwall et al., Phys. Rev. C **89**, 044310 (2014)
21. F. Brandolini, R.V. Ribas, Nucl. Instr. Meth. A **417**, 150 (1998)
22. A. Gavron et al., Phys. Rev. C **21**, 230 (1980)
23. D. Bourgin et al., Phys. Rev. C **90**, 044610 (2014)
24. C. Wells, N. Johnson, ORNL Rep. **6689**, 44 (1991)
25. R. Bhattacharjee et al., Phys. Rev. C **90**, 044319 (2014)
26. www.srim.org. Accessed 12 Nov 2020
27. J.F. Ziegler, J.P. Biersack, U. Littmark, *The stopping and range of ions in matter* (Pergamon, New York, 1985)
28. A. Jungclaus et al., Nucl. Phys. A **637**, 346 (1998)
29. A. Jungclaus, D. Kast, K.P. Lieb, C. Teich, M. Weiszflog et al., Phys. Rev. C **60**, 014309 (1999)
30. L.S. Northcliffe, R.F. Schilling, Atom. Data Nucl. Data Tab. **7**, 233 (1970)
31. Y. Qian, C. Qi, Phys. Rev. C **98**, 061303 (2018)
32. T. Bäck, C. Qi, B. Cederwall, R. Liotta, F. Ghazi Moradi, A. Johnson, R. Wyss, R. Wadsworth, Phys. Rev. C **87**, 031306(R) (2013)
33. C. Qi, Phys. Rev. C **94**, 034310 (2016)
34. C. Qi, unpublished